Report

Neuron

Spontaneous Infra-slow Brain Activity Has Unique Spatiotemporal Dynamics and Laminar Structure

Graphical Abstract

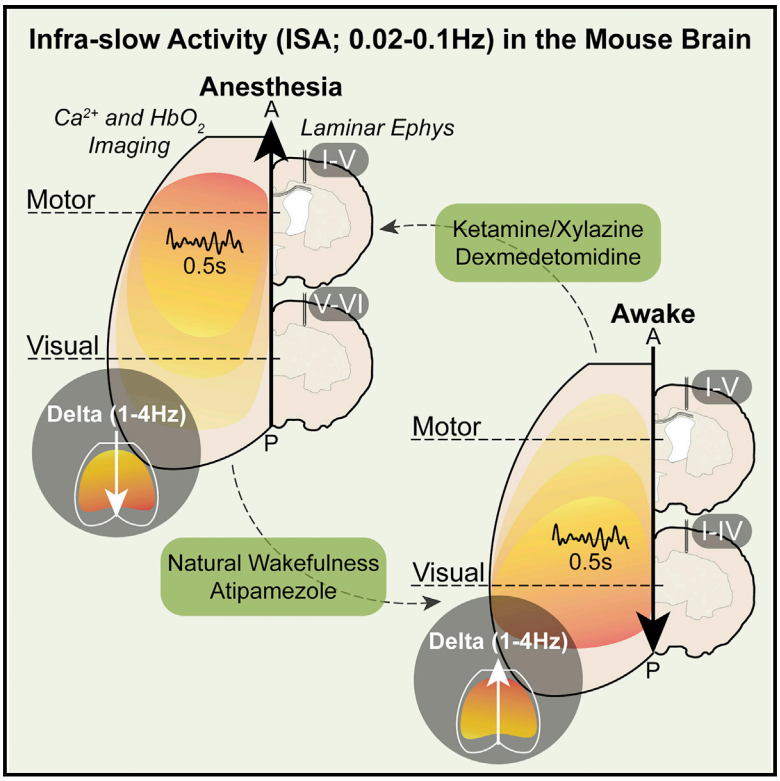

Highlights

- Wide-field Ca/hemoglobin imaging reveals infra-slow spatiotemporal trajectories
- Infra-slow activity (ISA) has distinct dynamics compared to higher frequencies
- The direction of ISA trajectories depends on state of consciousness
- Laminar electrophysiology shows that ISA travels through distinct cortical layers

Authors

Anish Mitra, Andrew Kraft, Patrick Wright, ..., Joseph Culver, Jin-Moo Lee, Marcus E. Raichle

Correspondence

anishmmitra@gmail.com

In Brief

Mitra et al. measure spontaneous infra-slow activity (ISA; <0.1 Hz) in mouse cortex using wide-field optical calcium/hemoglobin imaging and laminar electrophysiology. They find wide-scale cortical spatiotemporal trajectories in ISA that are state-dependent and distinct from higher frequency neural activity.

Mitra et al., 2018, Neuron *98*, 297–305
April 18, 2018
https://doi.org/10.1016/j.neuron.2018.03.015

CellPress

Neuron
Report

Spontaneous Infra-slow Brain Activity Has Unique Spatiotemporal Dynamics and Laminar Structure

Anish Mitra,[1,4,5,*] Andrew Kraft,[2,4] Patrick Wright,[1,4] Benjamin Acland,[3] Abraham Z. Snyder,[1,2] Zachary Rosenthal,[2] Leah Czerniewski,[2] Adam Bauer,[1] Lawrence Snyder,[2,3] Joseph Culver,[1] Jin-Moo Lee,[2] and Marcus E. Raichle[1,2]
[1]Department of Radiology, Washington University School of Medicine, St. Louis, MO, USA
[2]Department of Neurology, Washington University School of Medicine, St. Louis, MO, USA
[3]Department of Neuroscience, Washington University School of Medicine, St. Louis, MO, USA
[4]These authors contributed equally
[5]Lead Contact
*Correspondence: anishmmitra@gmail.com
https://doi.org/10.1016/j.neuron.2018.03.015

SUMMARY

Systems-level organization in spontaneous infra-slow (<0.1Hz) brain activity, measured using blood oxygen signals in fMRI and optical imaging, has become a major theme in the study of neural function in both humans and animal models. Yet the neurophysiological basis of infra-slow activity (ISA) remains unresolved. In particular, is ISA a distinct physiological process, or is it a low-frequency analog of faster neural activity? Here, using whole-cortex calcium/hemoglobin imaging in mice, we show that ISA in each of these modalities travels through the cortex along stereotypical spatiotemporal trajectories that are state dependent (wake versus anesthesia) and distinct from trajectories in delta (1–4 Hz) activity. Moreover, mouse laminar electrophysiology reveals that ISA travels through specific cortical layers and is organized into unique cross-laminar temporal dynamics that are different from higher frequency local field potential activity. These findings suggest that ISA is a distinct neurophysiological process that is reflected in fMRI blood oxygen signals.

INTRODUCTION

Imaging of spontaneous brain activity, from human resting state functional magnetic resonance imaging (rs-fMRI) to murine optical imaging, reveals long-distance relationships in the absence of explicit input or output (Biswal et al., 1995; Chan et al., 2015; Kenet et al., 2003; Ma et al., 2016). Initially dismissed as noise or artifact, the long-distance organization of spontaneous low-frequency activity is now widely studied. Spontaneous infra-slow (<0.1 Hz) fluctuations in the blood oxygen level-dependent (BOLD) signal are of particular interest because they are correlated within large task-associated systems (Fox and Raichle, 2007), because they recapitulate correlations in infra-slow electrophysiology (He et al., 2008), and finally, because BOLD signal correlations (functional connectivity; FC) have been related to a wide array of neuropsychiatric conditions (Greicius, 2008).

Yet despite the popularity of rs-fMRI as a method for studying brain function, the biology underlying spontaneous patterns in BOLD signals and infra-slow brain activity is not well understood. One prominent viewpoint posits that synchronization is an inherent property of connected neural networks; therefore, high-frequency neural activity naturally tends toward synchrony within structurally connected large-scale networks (Honey et al., 2009). In this model, infra-slow phenomena are viewed as a broad summation of fast, local neural activity (Breakspear, 2017). BOLD signals in particular are thought to reflect a vascular low-pass filtering of higher frequency neural activity (de Zwart et al., 2005). However, simulations modeling spontaneous BOLD signal organization as low-pass filtered action potentials synchronized through known white matter connections yield only modest agreement with measured BOLD signal correlations (Honey et al., 2009). Furthermore, a simple connectivity-synchrony model cannot readily explain dramatic state changes in infra-slow functional organization, such as in wake versus sleep (Mitra et al., 2015b).

As an alternative, rather than representing a broad summation of higher frequencies, the wide-scale organization of infra-slow activity (ISA) might instead reflect a distinct brain process with its own functional and neurophysiological principles (Breakspear, 2017). In support of this view, recent studies in humans (Mitra et al., 2014, 2015a) and mice (Matsui et al., 2016) have reported that infra-slow BOLD signals travel slowly through the cerebral cortex along stereotypical spatiotemporal trajectories. Spontaneous BOLD signals have also previously been linked to ISA in local field potentials (LFPs) (He et al., 2008; Leopold et al., 2003; Pan et al., 2013). Together, these findings suggest the possibility of a distinct infra-slow brain process that moves dynamically through the brain to establish a systems-level organization that is reflected in BOLD signals. However, key questions remain unanswered.

First, is the neurophysiology of ISA, especially its spatiotemporal trajectory through the cortex, distinct from other frequencies such as delta (1–4 Hz) activity? Frequencies below delta (or slow) activity (Steriade et al., 1993) are rarely examined in neurophysiology; thus, differentiating ISA from delta is necessary to show that ISA is a distinct entity. Second, do

spatiotemporal trajectories in BOLD signals correspond specifically to infra-slow neural activity, or do they reflect higher frequency spatiotemporal trajectories? Third, does the temporal organization of ISA have behavioral correlates, for example, by changing across broad behavioral states? Finally, distinct spectral bands such as gamma (>40 Hz), alpha (8–12 Hz), and delta are known to travel through specific layers of the cortex (Stroh et al., 2013; van Kerkoerle et al., 2014): does ISA travel through specific cortical layers as well? Importantly, this fourth question raises the possibility that rs-fMRI FC reflects heretofore unsuspected laminar specificity.

We explore these questions by using wide-field calcium/hemoglobin (Hgb) optical imaging and laminar electrophysiology in awake and anesthetized mice to directly measure and analyze the spatiotemporal structure of infra-slow and higher frequency spontaneous neural activity. To preview, we find that spontaneous ISA travels through stereotyped spatiotemporal trajectories in the mouse cortex that are distinct from higher frequencies.

RESULTS

Stability of FC over Frequencies and State

We first acquired concurrent wide-field calcium and Hgb imaging in 14 transgenic mice expressing GCaMP6f under control of a *Thy1* promoter (Figures 1A and S1). Imaging was acquired in a "resting state": mice were stationary, suspended in a hammock in a dark room with eyes open, and not subjected to any imposed experimental condition (STAR Methods). Spontaneous activity was imaged across consciousness states including wakefulness (n = 14), ketamine (ket)/xylazine anesthesia (n = 14), and dexmedetomidine (dex) anesthesia (n = 7). Ket and dex induce anesthesia through distinct mechanisms (Alkire and Miller, 2005; Nelson et al., 2003).

As the kinetics of calcium imaging measures neural activity up to ~5 Hz (Ma et al., 2016), we focused our analysis on infra-slow (0.02–0.1 Hz) and delta (1–4 Hz) activity, using FC and temporal delay (TD) (Figures 1B and 1C). Both measures are derived from lagged correlations between pairs of time series (STAR Methods; Mitra et al., 2014). FC is zero-lag correlation and TD is the temporal offset corresponding to the peak correlation. Temporal offsets measure lead-lag relationships between regions, allowing us to detect spatiotemporal trajectories in spontaneous activity. The matrices in Figures 1D and 1E (dimensions pixels × pixels) illustrate FC and TD between all pairs of cortical calcium time series. FC matrices in Figure 1D show that the correlation structure of spontaneous activity is stable over a range of frequencies (ISA versus delta) and across states of consciousness (wake versus ket/dex anesthesia).

Distinct Spatiotemporal Trajectories in ISA and Delta

We next analyze TD matrices (Figure 1E) to consider whether spatiotemporal trajectories differ between infra-slow and delta band calcium activity. Patterns of blue and red in each TD matrix indicate temporally early and late pixels, respectively. TD matrices are significantly ($p < 0.001$; STAR Methods) different between the ISA and delta frequencies, as well as between anesthesia (ket/dex) and wake. In contrast, TD matrices across ket and dex are highly similar for ISA and delta activity (no statistical difference). Hence, spatiotemporal trajectories differ significantly across ISA and delta and between wake and anesthesia. The timescales vary as well, ranging from ±0.5 s in ISA to ±10 ms in delta activity. GCaMP6 TD matrices were highly reproducible across sessions and mice; a full analysis of reliability is found in Figure S2.

To further understand spatiotemporal trajectories in spontaneous activity, we computed lag projections (images 1–6; Figure 2A), which are row-wise means of TD matrices (images 1–6; Figure 1E). Lag projections depict the degree to which, on average, each pixel is early (blue) or late (red) compared to the rest of the cortex. Hence, image 1 of Figure 2A illustrates that, on average, under ket anesthesia, anterior delta leads posterior delta by ~100 ms, consistent with prior reports of anterior-posterior propagation of delta activity in anesthesia and sleep (Massimini et al., 2004; Stroh et al., 2013). In contrast, posterior ISA leads anterior ISA by ~0.5 s (image 2; Figure 2A). Dex anesthesia (images 3 and 4 in Figure 2A) yields highly similar results. During wake, delta and ISA exhibit back-to-front and front-to-back spatiotemporal trajectories, respectively, again at very different timescales (images 3 and 4 in Figure 2A). In sum, Figure 2A illustrates that spontaneous ISA and delta, measured using GCaMP6 fluorescence, travel in distinct trajectories at different speeds. Moreover, both ISA and delta change directions across wake versus anesthesia.

Spatiotemporal Trajectories in Blood Oxygen Signals Recapitulate ISA, but Not Delta

To investigate how BOLD activity compares to infra-slow and delta calcium activity, we repeated the analyses in Figure 2A with Hgb signals (Figure 2B). ISA lag projections for total Hgb and calcium (GCaMP6) are highly similar (images 2, 4, and 6 in Figures 2A and 2B), consistent with prior reports of correspondence between infra-slow neural activity and hemodynamic signals (Huang et al., 2014; Leopold et al., 2003; Pan et al., 2013). However, delta frequency total Hgb lag projections do not match delta band calcium signals (images 1, 3, and 5 in Figures 2A and 2B) and are not reproducible (Figure S2). Analysis of oxy-Hgb and deoxy-Hgb yields concordant findings (Figure S1). Thus, the correspondence of Hgb and calcium spatiotemporal trajectories is limited to infra-slow frequencies.

Reciprocal Directionality and State Reversals in ISA and Delta Activity

The TD analyses in Figure 2A suggest that ISA and delta band calcium signals travel in reciprocal directions along the anterior-posterior axis of the mouse cortex, and that both ISA and delta trajectories reverse direction between wake and anesthesia. To test this idea, we analyzed Granger causality (GC) between two regions of interest (ROIs) in motor and visual cortices. Visual and motor ROIs were defined by identifying regions of maximal lag differences across wake and anesthesia and were used to quantify directionality along the anterior-posterior axis of cortex. Figure 2C shows GC for visual and motor calcium time series filtered into delta and ISA. GC reveals statistically significant Granger causation in the same direction as the

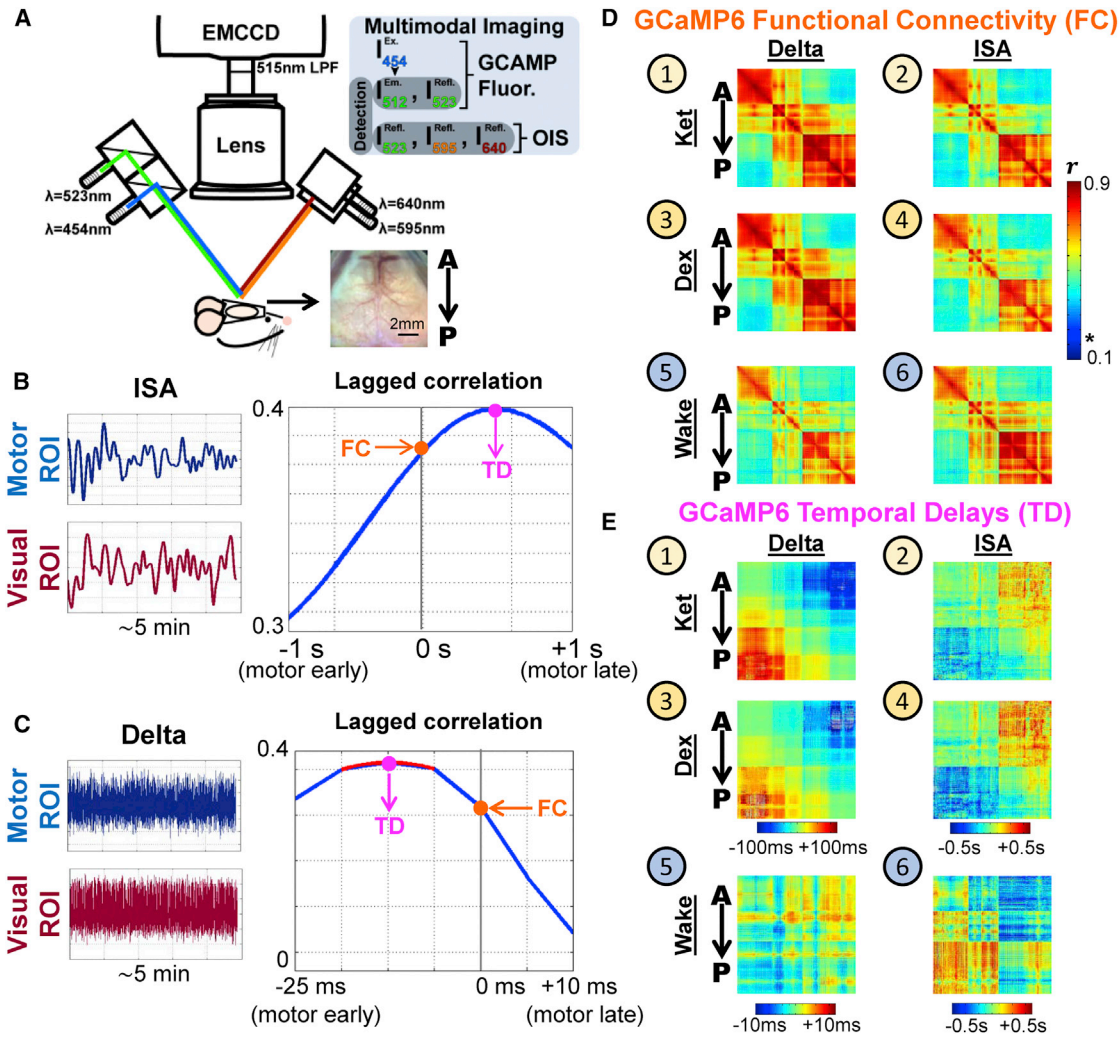

Figure 1. Correlations and TDs in Wide-Field Imaging of Spontaneous Calcium Activity in Mouse Cortex

(A) Calcium fluorescence and Hgb absorbance were concurrently imaged in the dorsal cortical surface of *Thy1*/GCaMP6 mice using four high-power LEDs (STAR Methods).

(B) An example lagged correlation curve computed using two infra-slow activity (ISA) time series from motor and visual regions of interest (ROIs). The zero-lag correlation value defines functional connectivity (FC); time corresponding to the peak correlation defines the temporal delay (TD) for the ROI pair.

(C) Same as (B), but for delta band activity. See Figure S1 for cross-correlations visualized over longer timescales.

(D) FC matrices, illustrating correlations between all pixels, shown for delta and ISA, ketamine (ket) (n = 14) and dexmedetomidine (dex) (n = 7) anesthesia as well as wake (n = 14). FC matrices are by definition symmetric ($r_{i,j} = r_{j,i}$). The rows and columns of the matrix are individual pixels from the dorsal surface of the mouse cortex arranged from anterior to posterior (see Figure S1 for key). Pearson r values greater than the color bar asterisk are statistically significant ($p < 0.005$; STAR Methods).

(E) TD matrices representing the TD between every pair of pixels, where the matrices are organized as in (D). TD matrices are by definition antisymmetric ($\tau_{i,j} = -\tau_{j,i}$). Non-significant TDs ($p > 0.005$; STAR Methods) are gray.

lag projections in Figure 2A. Thus, GC shows that ISA and delta travel in reciprocal anterior-posterior cortical directions, and that directionality in both frequency bands reverses across wake and ket/dex anesthesia.

We next computed phase delays over 0.02–5.12 Hz in double octaves (STAR Methods) between visual and motor ROIs (Figure 2C) to look for the spectral transition point between ISA and delta directionality. The result (Figure 2D) illustrates that phase offsets are stable over 0.02–0.32 Hz and over 1–5 Hz with a sharp directionality transition at ~0.64 Hz, in both wakefulness and ket anesthesia (dex behaves similarly; Figure S3). These results are not consistent with the hypothesis that infra-slow phase shifts are a low-pass filtered version of delta phase relationships, as this would produce a linear phase-frequency relationship.

To extend the concept behind Figure 2D to the whole cortex, we computed whole-cortex TD matrices (as in Figure 1E) for calcium signals filtered into double-octave frequency bins. We then computed the similarity between all pairs of TD matrices using rank-order correlations (Figure 3). This computation compares

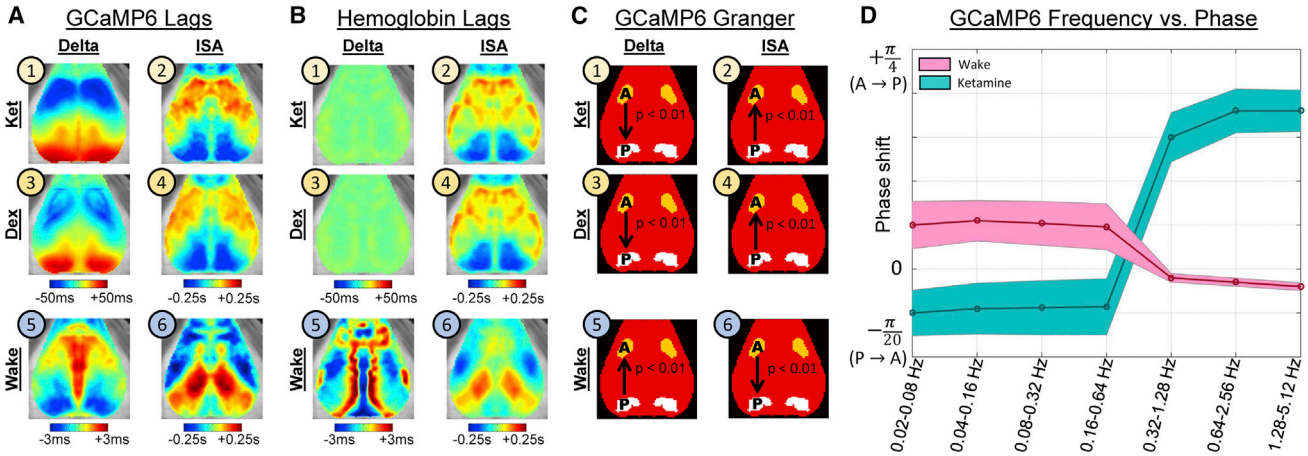

Figure 2. Spontaneous Spatiotemporal Trajectories Systematically Differ across Frequencies and States of Consciousness

(A) GCaMP6 (calcium) lag projections illustrating the mean delay between each pixel and the rest of cortex. Infra-slow and delta activity move in different directions and at different speeds during both wake and anesthesia.

(B) Total Hgb lag maps, derived as in (A), with matching timescales.

(C) Granger causality analysis of GCaMP6 activity. Two ROIs in visual and motor cortices were defined by identifying regions of maximal lag in panels A1–A4; see STAR Methods for coordinates.

(D) Frequency versus phase analysis between the two ROIs in (C) in wake (pink) and ket anesthesia (green). Analysis of dex anesthesia yields highly similar results (Figure S3). Error bars represent a 95% confidence interval computed over mice.

spatiotemporal trajectories in calcium activity over double-octave frequency bins. During ket anesthesia and wake (Figures 3A and 3B), two blocks of high correlation are apparent, in the 0.02–0.32 Hz range and in the 0.64–5 Hz range. Thus, the whole-cortex analysis reveals only two spectral regimes of spatiotemporal trajectories over 0.02–5.12 Hz with a transition point at ~0.64 Hz. Additionally, infra-slow and delta TD matrices are anti-correlated, indicating that activity moves in roughly reciprocal directions across infra-slow versus delta frequency ranges.

The same approach also quantifies reversal of directionality across wake and ket anesthesia (Figure 3C). Infra-slow TD matrices are anti-correlated across wake and ket anesthesia, as are delta band TD matrices, illustrating directionality reversal across states. Moreover, ISA directionality during wake resembles delta directionality during ket anesthesia, and delta directionality during wake resembles ISA directionality during ket anesthesia (Figure 2A). Dex anesthesia yields similar results (Figure S3). Hence, ISA and delta travel in reciprocal directions within a state (anesthesia or wake; Figures 3A and 3B), and activity in each frequency band approximately reverses direction across states (Figure 3C). Phase-delay matrix analyses of the type in Figures 3A–3C yield nearly identical results (Figure S3).

Finally, we repeated the analyses in Figures 3A–3C with whole-cortex FC matrices (as in Figure 1D) to examine how FC varies across frequencies and state of consciousness. The result is that FC is highly stable over 0.02–5 Hz (Spearman rho values > 0.9) during both ket anesthesia (Figure 3D) and wake (Figure 3E). FC is also generally stable (Spearman rho values > 0.8) across ket anesthesia and wake (Figure 3F). Therefore, FC is less sensitive than spatiotemporal trajectories to frequency- and state-specific differences in spontaneous activity.

Laminar Specificity in Infra-Slow Spatiotemporal Dynamics

We next explored higher frequencies (>5 Hz) and the laminar organization of spontaneous activity by inserting two 16-channel depth electrodes in the visual and motor cortices of mice (n = 13; Figure 4A) to record wide-spectrum (0.02–100 Hz) LFPs. We acquired data from 16 recording sites from superficial to deep in motor cortex and 12 sites along the depth of visual cortex, as visual cortex is thinner than motor cortex. Visual and motor cortices were chosen to match our imaging analyses (Figure 2C), allowing us to compare directional results across optical imaging and electrophysiological recordings.

First, to determine whether the spatiotemporal trajectory of ISA differs from higher frequencies in LFP activity, we computed cross-laminar FC and TD matrices between visual and motor cortices. The results for ISA and delta are shown in Figures 4B and 4C, which illustrate 16 × 12 FC and TD matrices depicting laminar relationships between motor and visual cortices. It is evident that the cross-laminar FC and TD structures of ISA and delta are distinct ($p < 0.001$; STAR Methods) both from each other and across wake and ket anesthesia. Further, ISA cross-laminar relationships are also distinct as compared to higher frequencies up to gamma ($p < 0.001$; STAR Methods), as illustrated in Figure S4. These results show that the spatiotemporal structure of spontaneous ISA is unique not only when compared to delta activity, but also when compared to canonical LFP bands up to 100 Hz. Note Figure 4C only reports significant TDs ($p < 0.01$, Bonferroni-corrected; STAR Methods); non-significant results are gray.

Figures 4B and 4C further reveal which cortical layers ISA travels through and the laminar basis for ISA directionality reversal across wake and ket anesthesia. Under ket anesthesia (image 2; Figure 4C), ISA in layers II–V in motor cortex leads ISA

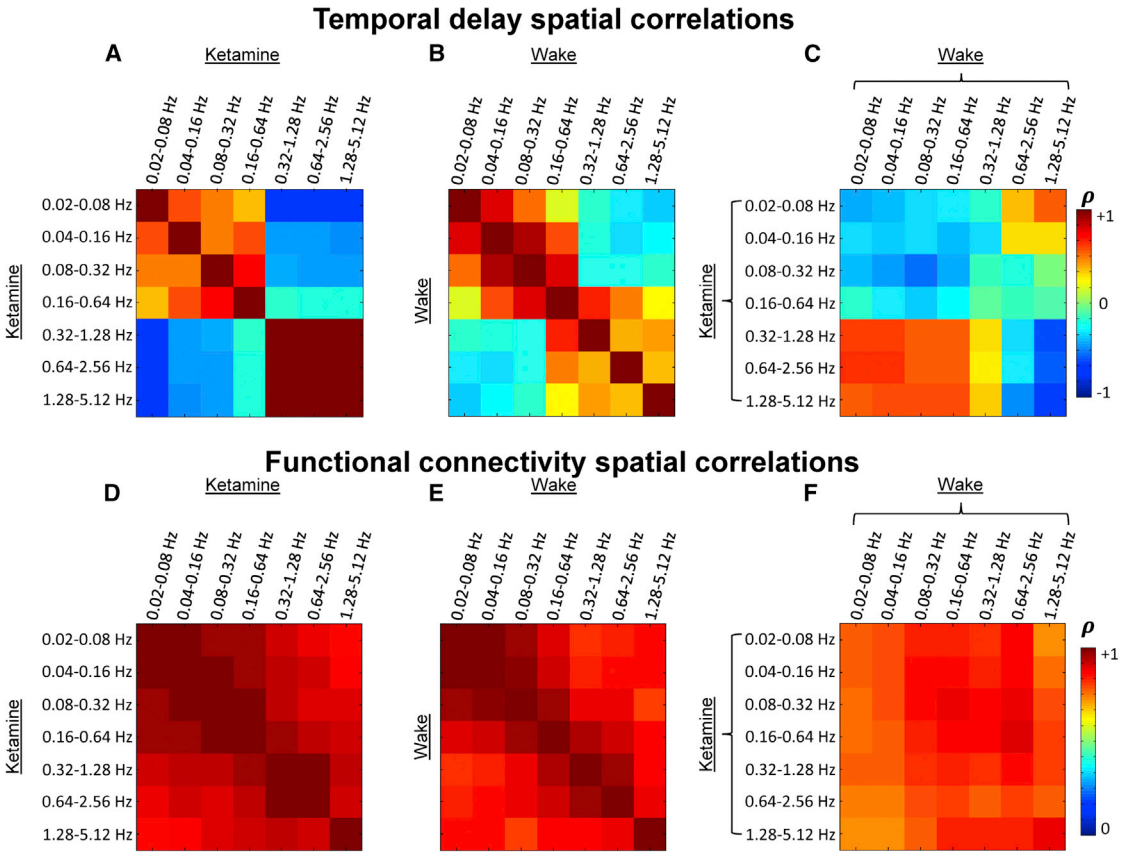

Figure 3. Comparison of Whole-Cortex Calcium Signal TD and FC Matrix Comparisons across Frequencies and States of Consciousness

(A–C) Each matrix entry reports the rank-order correlation between a pair of TD matrices, providing a quantitative comparison of spatiotemporal trajectories in calcium activity over double-octave frequency bins.

(A and B) Rank-order correlations between TD matrices across frequency bins in ket anesthesia (A) and wake (B).

(C) Rank-order correlations between anesthesia TD matrices and wake TD matrices.

(D–F) The same analyses as in (A)–(C), but now applied to FC matrices, providing quantitative comparison of correlation structure in calcium activity over double-octave frequency bins. Note difference in color bar scale between (A)–(C) and (D)–(F). Analysis of dex anesthesia yields highly similar results (Figure S3).

in layers II–IV in visual cortex (light blue). Conversely, ISA in deeper visual layers during ket anesthesia leads superficial/middle layers in motor cortex (red). The relative strength of signaling in each direction can be inferred from the correlation matrices. Comparing image 2 across Figures 4B and 4C, correlations corresponding to the red (visual-to-motor) temporal offsets are stronger than correlations corresponding to the blue (motor-to-visual) temporal offsets. Hence, for ISA under ket anesthesia, the visual-to-motor direction predominates, in accordance with calcium and Hgb imaging in Figure 2. The same reasoning shows the reverse during wake: the motor-to-visual direction predominates in infra-slow LFPs (image 4; Figures 4B and 4C), also in concordance with calcium and Hgb imaging.

Thus, on the basis of TDs, we find that ISA in ket anesthesia tends to travel from deep visual layers (V and VI) to most of motor cortical column (I–V). During wake, ISA tends to travel from layers I–V in motor cortex to layers I–IV in visual cortex; however, the shortest motor-visual lags are between layer V of motor cortex and layers I–IV of visual cortex (Figures 4C and 4D, image 4). Assuming the shortest TDs reflect the most direct relationships, we conclude that ISA tends to be sent from deep layers (V and VI) and received in more superficial layers (I–IV) during wake and ket anesthesia, as summarized in Figure 4D (panels 2 and 4).

FC and TD matrices computed in other frequency bands can also be analyzed similarly (Figure S4). For example, spontaneous delta activity moves from deep to superficial layers between visual and motor cortex and reverses directions across wake and ket anesthesia (Figure 4D), in agreement with our calcium imaging results. Just as in ISA, reversal of delta activity entails re-weighting ongoing bi-directional signaling, but the direction of delta activity is opposite that of ISA (Figure 4D, panels 1 and 3). Directionality reversal across wake and ket anesthesia is not observed for frequencies above delta (Figure S4). Analysis of dex anesthesia yields highly similar results to those found using ket anesthesia. Finally, computing FC and TD matrices using current source density time series recapitulates the results observed using LFPs (Figure S5).

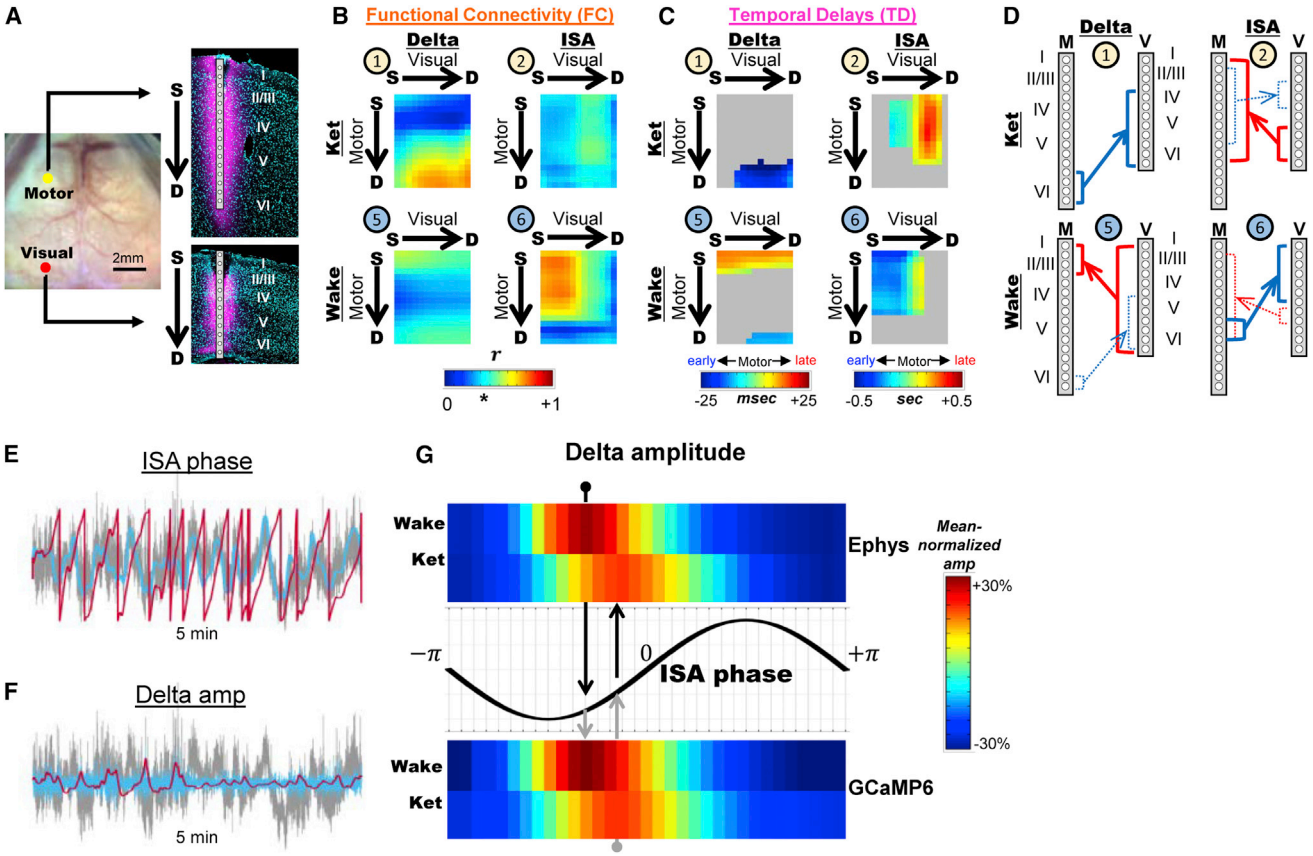

Figure 4. Cross-laminar Temporal Dynamics in Spontaneous Visual-Motor Activity Vary Systematically across Frequency and State

(A) Sixteen-channel depth probes were inserted into motor and visual cortices.

(B) Cross-laminar FC (n = 13). The four 16 × 12 matrices illustrate correlations between the 16 electrodes in motor cortex (rows) and the 12 electrodes in visual cortex (columns); electrodes are arranged from superficial to deep. Pearson r values greater than the color bar asterisk are statistically significant ($p < 0.001$; STAR Methods).

(C) Cross-laminar TD matrices (n = 13), arranged as in (B). Blue designates motor leading visual cortex; red indicates motor following visual cortex. Non-significant TDs ($p > 0.001$; STAR Methods) are gray.

(D) Schematic representation of the results in (B) and (C), highlighting the shortest delays between regions. Thick lines designate the predominant direction of signaling.

(E and F) Phase-amplitude coupling (PAC) between ISA phase and delta amplitude. Sample 5 min time series (gray) demonstrates ISA phase (E) and delta amplitude (F) are computed by first filtering (blue) and then applying a Hilbert transform (red).

(G) Delta amplitude is binned by infra-slow phase for each time series (electrode or pixel) and averaged. The resulting PAC histograms for electrophysiology and imaging, in wake and ket anesthesia, are highly concordant (see Figure S1 for PAC analysis of dex anesthesia).

Labels 1, 2, 5, and 6 correspond to the conditions in Figures 1 and 2. Figure S1 shows the dex anesthesia conditions corresponding to labels 3 and 4.

Spontaneous ISA Modulates Delta Activity

Finally, although ISA and delta have distinct spatiotemporal trajectories, prior task-based work has shown cross-frequency interaction between ISA phase and delta amplitude (Monto et al., 2008). To explore whether this occurs spontaneously, we computed phase-amplitude coupling (PAC) between ISA phase and delta amplitude (Figures 4E–4G). PAC was computed over all electrodes in our electrophysiological recordings as well as separately over all pixels in calcium imaging. In both cases, there is a robust, statistically significant ($p < 0.001$; STAR Methods) relationship between ISA phase and delta amplitude, and the phase of this relationship shifts between wake and ket anesthesia. Dex anesthesia yields highly similar results (Figure S1).

DISCUSSION

In summary, we find that spontaneous infra-slow brain activity follows consistent spatiotemporal trajectories between specific layers of the mouse cerebral cortex; the spatiotemporal and cross-laminar organization of spontaneous ISA differs from both delta activity and LFPs up to 100 Hz. Furthermore, the direction of ISA travel depends on the state (awake versus anesthetized) of the brain. In each state, the direction and topography of ISA spatiotemporal trajectories are concordant across Hgb imaging, calcium imaging, and electrophysiology. Taken together, these results support the view that there is a distinct infra-slow neurophysiological process whose temporal structure is state dependent. Moreover, blood oxygen signals specifically

correspond to the spatiotemporal dynamics and laminar organization of infra-slow brain activity.

Implications for Infra-Slow Neurophysiology

Infra-slow fluctuations in LFPs have been observed for decades (Aladjalova, 1957), but there is an ongoing debate about whether very low-frequency brain activity at broad spatial scales should be understood as a simple summation of local higher frequency events, or whether there are emergent organizational principles of ISA that differ from faster finer scale activities (Breakspear, 2017). Similar correlation structure (FC) between ISA and higher frequencies (Chan et al., 2015; Silasi et al., 2016) has been previously reported and used to argue that ISA represents a broad, slow summation of faster phenomena.

In this study, we too observed that the correlation structure of wide-scale calcium imaging is stable over 0.02–5 Hz; however, our analysis of spatiotemporal trajectories offers clear distinctions between ISA and higher frequency bands. Whole-cortex spatiotemporal trajectories in delta band activity, the closest canonical frequency band to ISA, are revealed by calcium imaging to differ significantly from the spatiotemporal dynamics of ISA during wake and anesthesia. Moreover, the cross-laminar spatiotemporal structure of ISA measured using electrophysiology, computed between mouse visual and motor cortices, differs from both delta band and higher frequency LFPs up to 100 Hz. Future technologies that allow wide-scale measurement of full-spectrum activity may offer even greater detail about the differences between ISA and higher frequencies, but the present work clearly demonstrates that the spatiotemporal dynamics of ISA do not map onto higher frequencies.

The principle that ISA has its own functional and neurophysiological properties that are distinct from higher frequencies represents a low-frequency extension of concepts advanced by Steriade and others, who have demonstrated that the slow delta oscillation is a unique brain process (Steriade et al., 1993) that moves through specific cortical layers (Stroh et al., 2013) as well as cortico-thalamic loops (Sheroziya and Timofeev, 2014) and is involved in memory consolidation (Marshall et al., 2006). The present work illustrates some analogous properties in ISA: the spatiotemporal dynamics of ISA are unique compared to higher frequencies and ISA tends to travel from deep cortical layers to more superficial ones (Figure 4), at least between visual and motor cortices. Spread of low-frequency spontaneous activity from deep layers is consistent with prior work (Sakata and Harris, 2009). Furthermore, the spatiotemporal organization of ISA appears linked to the state of the brain (see State Dependence). However, several questions remain regarding the unique properties of ISA: for example, the cortical relationships established in this paper do not preclude a role for subcortical connections (Xiao et al., 2017) (much as delta activity involves cortico-cortical and cortico-thalamic connections). Future work must also address the origins of infra-slow phenomena, with possible roles for recurrent polysynaptic connectivity (Deco et al., 2017), subthreshold activity (Berger et al., 2007; Kavalali et al., 2011), and glial metabolic signaling (Poskanzer and Yuste, 2011). Finally, the present observation of consistent spatiotemporal trajectories in ISA should not be mistaken for "information flow"; instead, it is more likely that ISA shapes or modulates higher frequency information processing in the brain (Mitra et al., 2016), a hypothesis that must be tested in future studies.

Implications for BOLD Imaging

rs-fMRI is generally interpreted as representing a broad summary of neural activity, on the assumption that BOLD signals reflect a vascular low-pass filtering of higher frequency neural activity (de Zwart et al., 2005; Honey et al., 2009). We show that infra-slow spatiotemporal trajectories in blood oxygen signals agree specifically with ISA spatiotemporal dynamics derived using calcium imaging (Figure 2) and electrophysiology (Figure 4). Since neurophysiological measures distinguish infra-slow spatiotemporal dynamics from higher frequencies, we conclude that the organization of spontaneous BOLD signals is specifically attributable to an infra-slow brain process. Furthermore, our finding that spontaneous ISA travels from deep to superficial cortical layers between visual and motor cortices (Figure 4) implies that long-distance BOLD signal relationships reflect a previously unappreciated degree of laminar specificity. These results establish an expanded basis for interpreting the neurophysiology of long-distance relationships in rs-fMRI.

Our findings are also relevant to ongoing investigations of dynamics in blood oxygen signals and their relationships to states of brain function. The vast majority of the rs-fMRI dynamics literature has focused on changes in infra-slow zero-lag correlation structure over time (Liégeois et al., 2017). Our results address dynamics from the perspective of infra-slow spatiotemporal trajectories and demonstrate that these trajectories are far more labile across wake and anesthetized states than are zero-lag correlation matrices (Figures 2 and 3). Therefore, the dynamical organization of rs-fMRI and its relation to brain states may manifest more fundamentally in spatiotemporal trajectories than changes in correlation structure.

Relationship between ISA and Delta Activity

Although the spatiotemporal organization of ISA and delta is distinct, two of the present findings suggest that spontaneous activity in these two spectral regimes is nonetheless functionally linked. First, ISA and delta travel in approximately reciprocal directions along the anterior-posterior axis of the dorsal mouse cortex (Figure 2E). We have previously observed delta and ISA traveling in reciprocal directions between the human hippocampus and cerebral cortex (Mitra et al., 2016) and hypothesized that this was a feature of cortico-hippocampal communication. Our present results in the mouse suggest, instead, that reciprocal travel of delta and ISA occurs more broadly. A possible function of this reciprocal travel is the conveyance of slow (delta) feedforward and slower (ISA) feedback influences, analogous to what has been observed for gamma and alpha activity in the visual cortex during visual tasks (van Kerkoerle et al., 2014), although the concepts of feedforward and feedback must be expanded to address spontaneous activity.

Second, the phase of ISA is coupled with the amplitude of delta band activity in both calcium and electrophysiological recordings (this phase relationship shifts slightly across states of consciousness; Figures 4 and S1). Prior work has also shown that ISA modulates the amplitude of frequencies higher than delta during tasks (Monto et al., 2008). On this basis, we

speculate that spontaneous activity may be hierarchically organized by frequency, such that ISA modulates power in higher frequencies.

State Dependence

We find reversals in the prevailing direction of spatiotemporal trajectories across wake and anesthesia, in both delta and ISA (Figures 2, 3, and 4). This reversal of directionality is not observed in higher frequencies (Figures S4 and S5). We therefore hypothesize that the temporal structure of low-frequency activity, especially its direction of cortical travel, plays a special role in governing or marking functional brain states. This conclusion is further supported by supplemental experiments demonstrating that administration of a dex reversal agent (atipamezole) during dex anesthesia not only rapidly re-establishes wakefulness in dex anesthetized mice, but also re-establishes waking ISA and delta activity patterns (Figures S1, S3, and S5). Future work examining a wider variety of pharmacological agents and physiological states will be necessary to determine commonalities and differences in low-frequency activity patterns across various conditions, including possible differences between states in which animals are freely moving versus the stationary eyes-open resting state.

Finally, our laminar electrophysiology findings also suggest that, mechanistically, the reversal of the predominant direction of travel in ISA and delta activity is accomplished by changing the relative weighting of bi-directional signaling in distinct cross-laminar relationships (Figure 4D). The basis of this reweighting requires further investigation, but it is natural to suggest that neuromodulation may play a role in directionality shifts across wake versus anesthesia (Marder, 2012).

STAR★METHODS

Detailed methods are provided in the online version of this paper and include the following:

- KEY RESOURCES TABLE
- CONTACT FOR REAGENT AND RESOURCE SHARING
- EXPERIMENTAL MODEL AND SUBJECT DETAILS
  - Animal Subjects
- METHOD DETAILS
  - Animal Preparation for Optical Imaging
  - Animal Preparation for Electrophysiology
  - Optical Imaging System
  - Electrophysiology System
  - Awake Recordings
  - Anesthetized Recordings
  - Epifluorescence and Confocal Imaging
- QUANTIFICATION AND STATISTICAL ANALYSIS
  - Image Processing
  - Electrophysiology Signal Processing
  - Correlation and Temporal Lags
  - Group-level FC and TD matrices
  - Group-level Phase-frequency Plots
  - Group-level Granger Causality (GC)
  - Current Source Density
  - Statistical Significance

SUPPLEMENTAL INFORMATION

Supplemental Information includes six figures and can be found with this article online at https://doi.org/10.1016/j.neuron.2018.03.015.

ACKNOWLEDGMENTS

This work was funded by the NIH (F30MH106253 to A.M.; NS080675 to M.E.R.; R01NS084028, R01NS085419, and R01NS094692 to J.-M.L.; F31NS089135 to A.K.; MH102471 to L.S.; and R01 NS099429 and R01 NS078223 to J.C.) and the McDonnell Center for Systems Neuroscience. We thank Manu Goyal and John McCarthy for helpful discussions.

AUTHOR CONTRIBUTIONS

A.M. and M.E.R. conceptualized and drafted the paper; A.M., A.K., B.A., P.W., Z.R., A.B., and L.C. performed the experiments; A.M. analyzed the data; and A.M., A.K., B.A., P.W., A.Z.S., Z.R., A.B., L.S., J.C., J.-M.L., and M.E.R. reviewed and edited the final paper.

DECLARATION OF INTERESTS

The authors declare no competing interests.

Received: September 9, 2017
Revised: January 28, 2018
Accepted: March 8, 2018
Published: March 29, 2018

REFERENCES

Aladjalova, N.A. (1957). Infra-slow rhythmic oscillations of the steady potential of the cerebral cortex. Nature *179*, 957–959.

Alkire, M.T., and Miller, J. (2005). General anesthesia and the neural correlates of consciousness. Prog. Brain Res. *150*, 229–244.

Barnett, L., and Seth, A.K. (2014). The MVGC multivariate Granger causality toolbox: a new approach to Granger-causal inference. J. Neurosci. Methods *223*, 50–68.

Berger, T., Borgdorff, A., Crochet, S., Neubauer, F.B., Lefort, S., Fauvet, B., Ferezou, I., Carleton, A., Lüscher, H.R., and Petersen, C.C. (2007). Combined voltage and calcium epifluorescence imaging in vitro and in vivo reveals subthreshold and suprathreshold dynamics of mouse barrel cortex. J. Neurophysiol. *97*, 3751–3762.

Biswal, B., Yetkin, F.Z., Haughton, V.M., and Hyde, J.S. (1995). Functional connectivity in the motor cortex of resting human brain using echo-planar MRI. Magn. Reson. Med. *34*, 537–541.

Breakspear, M. (2017). Dynamic models of large-scale brain activity. Nat. Neurosci. *20*, 340–352.

Canolty, R.T., Edwards, E., Dalal, S.S., Soltani, M., Nagarajan, S.S., Kirsch, H.E., Berger, M.S., Barbaro, N.M., and Knight, R.T. (2006). High gamma power is phase-locked to theta oscillations in human neocortex. Science *313*, 1626–1628.

Chan, A.W., Mohajerani, M.H., LeDue, J.M., Wang, Y.T., and Murphy, T.H. (2015). Mesoscale infraslow spontaneous membrane potential fluctuations recapitulate high-frequency activity cortical motifs. Nat. Commun. *6*, 7738.

de Zwart, J.A., Silva, A.C., van Gelderen, P., Kellman, P., Fukunaga, M., Chu, R., Koretsky, A.P., Frank, J.A., and Duyn, J.H. (2005). Temporal dynamics of the BOLD fMRI impulse response. Neuroimage *24*, 667–677.

Deco, G., Kringelbach, M.L., Jirsa, V.K., and Ritter, P. (2017). The dynamics of resting fluctuations in the brain: metastability and its dynamical cortical core. Sci. Rep. *7*, 3095.

Fox, M.D., and Raichle, M.E. (2007). Spontaneous fluctuations in brain activity observed with functional magnetic resonance imaging. Nat. Rev. Neurosci. *8*, 700–711.

Greicius, M. (2008). Resting-state functional connectivity in neuropsychiatric disorders. Curr. Opin. Neurol. *21*, 424–430.

He, B.J., Snyder, A.Z., Zempel, J.M., Smyth, M.D., and Raichle, M.E. (2008). Electrophysiological correlates of the brain's intrinsic large-scale functional architecture. Proc. Natl. Acad. Sci. USA *105*, 16039–16044.

Honey, C.J., Sporns, O., Cammoun, L., Gigandet, X., Thiran, J.P., Meuli, R., and Hagmann, P. (2009). Predicting human resting-state functional connectivity from structural connectivity. Proc. Natl. Acad. Sci. USA *106*, 2035–2040.

Huang, L., Liu, Y., Li, M., and Hu, D. (2014). Hemodynamic and electrophysiological spontaneous low-frequency oscillations in the cortex: directional influences revealed by Granger causality. Neuroimage *85*, 810–822.

Kavalali, E.T., Chung, C., Khvotchev, M., Leitz, J., Nosyreva, E., Raingo, J., and Ramirez, D.M. (2011). Spontaneous neurotransmission: an independent pathway for neuronal signaling? Physiology (Bethesda) *26*, 45–53.

Kenet, T., Bibitchkov, D., Tsodyks, M., Grinvald, A., and Arieli, A. (2003). Spontaneously emerging cortical representations of visual attributes. Nature *425*, 954–956.

Leopold, D.A., Murayama, Y., and Logothetis, N.K. (2003). Very slow activity fluctuations in monkey visual cortex: implications for functional brain imaging. Cereb. Cortex *13*, 422–433.

Liégeois, R., Laumann, T.O., Snyder, A.Z., Zhou, J., and Yeo, B.T.T. (2017). Interpreting temporal fluctuations in resting-state functional connectivity MRI. Neuroimage *163*, 437–455.

Ma, Y., Shaik, M.A., Kozberg, M.G., Kim, S.H., Portes, J.P., Timerman, D., and Hillman, E.M. (2016). Resting-state hemodynamics are spatiotemporally coupled to synchronized and symmetric neural activity in excitatory neurons. Proc. Natl. Acad. Sci. USA *113*, E8463–E8471.

Marder, E. (2012). Neuromodulation of neuronal circuits: back to the future. Neuron *76*, 1–11.

Marshall, L., Helgadóttir, H., Mölle, M., and Born, J. (2006). Boosting slow oscillations during sleep potentiates memory. Nature *444*, 610–613.

Massimini, M., Huber, R., Ferrarelli, F., Hill, S., and Tononi, G. (2004). The sleep slow oscillation as a traveling wave. J. Neurosci. *24*, 6862–6870.

Matsui, T., Murakami, T., and Ohki, K. (2016). Transient neuronal coactivations embedded in globally propagating waves underlie resting-state functional connectivity. Proc. Natl. Acad. Sci. USA *113*, 6556–6561.

Mitra, A., Snyder, A.Z., Hacker, C.D., and Raichle, M.E. (2014). Lag structure in resting-state fMRI. J. Neurophysiol. *111*, 2374–2391.

Mitra, A., Snyder, A.Z., Blazey, T., and Raichle, M.E. (2015a). Lag threads organize the brain's intrinsic activity. Proc. Natl. Acad. Sci. USA *112*, E2235–E2244.

Mitra, A., Snyder, A.Z., Tagliazucchi, E., Laufs, H., and Raichle, M.E. (2015b). Propagated infra-slow intrinsic brain activity reorganizes across wake and slow wave sleep. eLife *4*, https://doi.org/10.7554/eLife.10781.

Mitra, A., Snyder, A.Z., Hacker, C.D., Pahwa, M., Tagliazucchi, E., Laufs, H., Leuthardt, E.C., and Raichle, M.E. (2016). Human cortical-hippocampal dialogue in wake and slow-wave sleep. Proc. Natl. Acad. Sci. USA *113*, E6868–E6876.

Monto, S., Palva, S., Voipio, J., and Palva, J.M. (2008). Very slow EEG fluctuations predict the dynamics of stimulus detection and oscillation amplitudes in humans. J. Neurosci. *28*, 8268–8272.

Nelson, L.E., Lu, J., Guo, T., Saper, C.B., Franks, N.P., and Maze, M. (2003). The alpha2-adrenoceptor agonist dexmedetomidine converges on an endogenous sleep-promoting pathway to exert its sedative effects. Anesthesiology *98*, 428–436.

Pan, W.J., Thompson, G.J., Magnuson, M.E., Jaeger, D., and Keilholz, S. (2013). Infraslow LFP correlates to resting-state fMRI BOLD signals. Neuroimage *74*, 288–297.

Poskanzer, K.E., and Yuste, R. (2011). Astrocytic regulation of cortical UP states. Proc. Natl. Acad. Sci. USA *108*, 18453–18458.

Sakata, S., and Harris, K.D. (2009). Laminar structure of spontaneous and sensory-evoked population activity in auditory cortex. Neuron *64*, 404–418.

Sheroziya, M., and Timofeev, I. (2014). Global intracellular slow-wave dynamics of the thalamocortical system. J. Neurosci. *34*, 8875–8893.

Shimaoka, D., Song, C., and Knöpfel, T. (2017). State-dependent modulation of slow wave motifs towards awakening. Front. Cell. Neurosci. *11*, 108.

Silasi, G., Xiao, D., Vanni, M.P., Chen, A.C., and Murphy, T.H. (2016). Intact skull chronic windows for mesoscopic wide-field imaging in awake mice. J. Neurosci. Methods *267*, 141–149.

Steriade, M., Nuñez, A., and Amzica, F. (1993). A novel slow (< 1 Hz) oscillation of neocortical neurons in vivo: depolarizing and hyperpolarizing components. J. Neurosci. *13*, 3252–3265.

Stroh, A., Adelsberger, H., Groh, A., Rühlmann, C., Fischer, S., Schierloh, A., Deisseroth, K., and Konnerth, A. (2013). Making waves: initiation and propagation of corticothalamic Ca2+ waves in vivo. Neuron *77*, 1136–1150.

van Kerkoerle, T., Self, M.W., Dagnino, B., Gariel-Mathis, M.A., Poort, J., van der Togt, C., and Roelfsema, P.R. (2014). Alpha and gamma oscillations characterize feedback and feedforward processing in monkey visual cortex. Proc. Natl. Acad. Sci. USA *111*, 14332–14341.

White, B.R., Bauer, A.Q., Snyder, A.Z., Schlaggar, B.L., Lee, J.M., and Culver, J.P. (2011). Imaging of functional connectivity in the mouse brain. PLoS ONE *6*, e16322.

Xiao, D., Vanni, M.P., Mitelut, C.C., Chan, A.W., LeDue, J.M., Xie, Y., Chen, A.C., Swindale, N.V., and Murphy, T.H. (2017). Mapping cortical mesoscopic networks of single spiking cortical or sub-cortical neurons. eLife *6*, https://doi.org/10.7554/eLife.19976.

STAR★METHODS

KEY RESOURCES TABLE

REAGENT or RESOURCE	SOURCE	IDENTIFIER
Chemicals, Peptides, and Recombinant Proteins		
Ketamine (86.9 mg/kg)	WUSTL Division of Comparative Medicine Veterinary Pharmacy	N/A
Xylazine (13.4 mg/kg)	WUSTL Division of Comparative Medicine Veterinary Pharmacy	N/A
Dexmedetomidine (0.5 mg/kg)	WUSTL Division of Comparative Medicine Veterinary Pharmacy	N/A
Atipamezole (0.5 mg/kg)	WUSTL Division of Comparative Medicine Veterinary Pharmacy	N/A
Experimental Models: Organisms/Strains		
Mouse: Thy1/GCaMP6f: C57BL/6J-Tg(Thy1-GCaMP6f)GP5.5Dkim	The Jackson Laboratories	https://www.jax.org/; JAX: 024276; RRID: IMSR_JAX:024276
Mouse: C57Bl6/J: C57Bl6/J	The Jackson Laboratories	https://www.jax.org/; JAX: 000664; RRID: IMSR_JAX:000664
Software and Algorithms		
MATLAB	MathWorks	https://www.mathworks.com/products/matlab.html; RRID: SCR_001622
Granger Causality MATLAB Toolbox	Barnett and Seth, 2014	https://users.sussex.ac.uk/~lionelb/MVGC/
Other		
Andor EMCCD	Andor Technology	http://www.andor.com/; iXon 897
NeuroNexus Electrodes	NeuroNexus	https://www.neuronexus.com; A1x16-5mm-100-703-A16

CONTACT FOR REAGENT AND RESOURCE SHARING

Further information and requests for resources and reagents should be directed to and will be fulfilled by the Lead Contact, Anish Mitra (anishmitra@wustl.edu).

EXPERIMENTAL MODEL AND SUBJECT DETAILS

Animal Subjects

All procedures described below were approved by the Washington University Animal Studies Committee in compliance with AAALAC guidelines. Imaging studies were performed on transgenic mice expressing GCaMP6f under control of a mouse *Thy1* promoter acquired from Jackson Laboratories (JAX Strain: C57BL/6J-*Tg(Thy1-GCaMP6f)GP5.5Dkim*; stock: 024276). GCaMP6/Thy1 transgenic genotypes were confirmed by PCR using the forward primer 5′-CATCAGTGCAGCAGAGCTTC-3′ and reverse primer 5′-CAGCGTATCCACATAGCGTA-3′. Histology of GCaMP6 fluorescence is shown in Figure S1. Electrophysiology studies were performed on C57Bl6/J mice (Jackson Laboratories; stock: 664). All mice were male, 12 to 16 weeks of age, weighed 28-36 g, and raised in standard cages in a dedicated mouse facility with a 12hr-12hr light/dark cycle.

METHOD DETAILS

Animal Preparation for Optical Imaging

Fourteen GCaMP6 mice (12-16 weeks of age, 28-36 g) were used for imaging in this study. Genetically modified GCaMP6 mice were studied solely for the purpose of optical calcium imaging, and were otherwise phenotypically normal. Mice were sedated with isoflurane (3% induction, 1% maintenance, 0.5 L/min) and placed in a stereotactic holder. The head was then shaved, and a midline

incision made to expose the skull. Body temperature was maintained at 37°C using a temperature controlled heating pad. Chronic cranial windows made of Plexiglas and with pre-tapped holes were fixed to the skull using dental cement (C&B-Metabond, Parkell, Edgewood, NY, USA).

Animal Preparation for Electrophysiology

Thirteen C57Bl6/J mice were used to obtain electrophysiological recordings. Mice were given dexamethasone (20 μL 4mg/mL, S.C.) 4 hours prior to surgery, and mannitol (150 μL, 20% manitol, I.P.) immediately prior to surgery. Mice were anesthetized using isoflurane anesthesia (3% induction, 1.5% maintenance). Once anesthetized, lidocaine anesthetic was given locally, scalp hair was removed, a midline incision was made in the scalp, and the scalp was retracted. The periosteal membranes were removed. Two craniectomies (1mm in diameter) were performed over the motor and visual locations determined by stereotactic coordinates derived from the Granger Causality analysis shown in Figure 2C (Motor cortex = 1.5 mm Left of bregma, 1.6 mm anterior to bregma; visual cortex = 2.6 mm Left of bregma, 3.0 mm posterior to bregma). A third craniotomy was made on the right hemisphere (2.3 mm Right of bregma, 0.9 mm anterior to bregma), and a permanent ground wire was placed and secured with C&B Metabond dental cement (Parkell, Edgewood, NY, USA). A custom-made fixation block with screw threading was attached to the skull with dental cement (to enable head fixation during recording). The left hemisphere craniectomies were covered with a self-healing silicone polymer that allowed silicone electrodes to pass through undamaged. Mice were given S.C. buprenorphine at the end of the procedure for pain control, and mice were given 5 days of recovery time before any recording was performed.

Optical Imaging System

Sequential illumination was provided by four LEDs: 470nm (measured peak λ = 454nm (referred to as 454nm LED in this study), LCS-0470-15-22, Mightex Systems, Pleasanton, CA, USA), 530nm (measured peak λ = 523nm, LCS-0530-15-22), 590nm (measured peak λ = 595nm, LCS-0590-10-22), and 625nm (measured peak λ = 640nm, LCS-0625-03-22). The 454nm LED is used for GCaMP excitation, and the 523nm, 595nm, and 640nm LEDs are used for multispectral oximetric imaging. The 523nm LED was also used as an emission reference for GCaMP6 fluorescence in order to remove any confound of hemodynamics in the fluorescence signal (described below). Both the 454nm and 523nm LED light paths were made collinear by using a multi-wavelength beam combiner dichroic mirror (LCS-BC25-0505, Mightex Systems, Pleasanton, CA, USA). For image detection, we used a cooled, frame-transfer EMCCD camera (iXon 897, Andor Technologies, Belfast, Northern Ireland, United Kingdom) in combination with an 85mm f/1.4 camera lens (Rokinon, New York, NY, USA). The acquisition framerate was 16.8Hz per channel, with the overall framerate of the camera as ~67Hz. This framerate is well above the temporal resolution necessary to adequately characterize hypothesized GCaMP6 activity. To increase frame rate as well as increase SNR, the CCD was binned at 4 × 4 pixels; this reduced the resolution of the output images from full-frame 512 × 512 pixels to 128 × 128 pixels. Both the LEDs and the exposure of the CCD were synchronized and triggered via a DAQ (PCI-6733, National Instruments, Austin, TX, USA) using MATLAB (MathWorks, Natick, MA, USA). The field-of-view was adjusted to be approximately 1 cm^2 resulting in an area that covered the majority of the convexity of the cerebral cortex with anterior-posterior coverage from the olfactory bulb to the superior colliculus. The resulting pixels were approximately 78μm x 78μm. To minimize specular reflection from the skull, we used a series of linear polarizers in front of the LED sources and the CCD lens. The secured mouse was placed at the focal plane of the camera. The combined, collimated LED unit was placed approximately 8 cm from the mouse skull, with a working distance of approximately 14cm as determined by the acquisition lens. A 515nm longpass filter (Semrock, Rochester, NY, USA) was placed in front of the CCD to filter out 470nm fluorescence excitation light and a 460/60nm bandpass filter (Semrock, Rochester, NY, USA) was used in front of the excitation source to further minimize leakage of fluorescence excitation light through the 515nm longpass filter. The pulse durations for the LEDs are 20ms, 5ms, 3ms, 1ms for 454nm, 523nm, 595nm, and 640nm, respectively.

Electrophysiology System

For electrophysiology recordings, mice were placed on a felt hammock and the skull was fixed to a secure bar via the fixation block. Two 1.5mm 16-channel linear array electrodes (NeuroNexus model number A1x16-5mm-100-703-A16, Ann Arbor, MI, USA) were attached to separate micromanipulators (David Kopf Instruments, Los Angeles, California, USA). Electrodes were painted with DiI (1,1'-Dioctadecyl-3,3,3′,3′-Tetramethylindocarbocyanine Perchlorate; Sigma-Aldrich, St. Louis, MO, USA), and placed into the brain (through the transparent silicone sealant which enabled direct visualization of the cortex) under direct visualization using a surgical stereoscope (Olympus, Tokyo, Japan). Electrode placement was confirmed in three ways: 1) the most superficial contact was visually guided to just under the cortical surface; 2) the electrophysiological signal in the most superficial contact during the transition from noise/air to brain was monitored 3) electrodes were painted with DiI and placement was confirmed with histologic sections of the mouse brain (Figure 4A). Local field potentials were recorded using an amplifier with high-pass filter cutoff of 0.02Hz (Intan RDH2132) connected to the recording computer through an acquisition board (OpenEphys), with a reference wire positioned on the right hemisphere contralateral to the electrodes (2.3 mm Right of bregma, 0.9 mm anterior to bregma). All recordings were made in a completely dark room. For each mouse, awake recordings were done first, followed by ketamine/xylazine administration via I.P. injection in the same session (i.e., without removing the electrodes from the brain).

Awake Recordings

As described in the electrophysiology system description, awake mouse recordings (imaging and electrophysiology) were performed by mice on a felt hammock with head-fixation, either to the optical window in the case of imaging or to the skull in the case of electrophysiology. The hammock provided a dark, comfortable environment while preventing the awake mouse from applying torque on their restrained head. After recovery from surgery, the mouse was acclimated to the hammock apparatus by a training period consisting of two 20 minute sessions. Acclimation is indexed by a return to normal behavior (e.g., whisking, grooming, and walking with head restrained). Though no accelerometers or other behavioral measures were used to track motion within the pouch during recordings, mice were qualitatively observed to be relaxed with infrequent limb motion after completion of the acclimation protocol. For 7 of the 14 mice, awake imaging was performed for 60 minutes on two separate days, separated by two weeks. For the remaining 7 mice, awake imaging was performed for 60 minutes on a single day. The 60 minute imaging sessions were acquired over 12 5-minute runs. Awake electrophysiology was acquired continuously for 60 minutes in 13 mice.

Anesthetized Recordings

For ketamine anesthetized imaging and electrophysiology, mice were anesthetized with I.P. injection of a ketamine/xylazine cocktail (86.9 mg/kg Ketamine, 13.4 mg/kg Xylazine). For dexmedetomidine imaging and electrophysiology, mice were anesthetized with I.P injection of dexmedetomidine (0.5 mg/kg). Anesthetic effect was verified by confirming that the animal was not responsive to a hind paw pinch. The animal was placed and kept on a solid state water circulating heating pad (T/Pump Classic, Stryker Co., Kalamazoo, MI, USA), maintained at 42°C. For 7 of the 14 mice, anesthetized imaging was performed for 45 minutes (the duration of anesthetic effect) on two separate days, separated by two weeks. In the remaining 7 mice, anesthetized imaging was performed for 45 minutes on a single day. The 45 minute imaging sessions were acquired over 9 5-minute runs. Anesthetized electrophysiology was acquired continuously for 45 minutes in 13 mice. We also collected data in which Dexmedetomidine anesthesia was instantaneously reversed with an intraperitoneal injection of atipamezole (0.5 mg/kg). Reversal of dexmedetomidine anesthesia (dex reversal) was confirmed by the resumption of mouse reflexes and typical waking behavior, such as whisking and grooming. 7 mice were imaged in the dex reversal condition for 45 minutes each; electrophysiology was obtained from 5 mice in the dex reversal condition for 45 minutes each.

Epifluorescence and Confocal Imaging

Mice were deeply anesthetized with FatalPlus (Vortech Pharmaceuticals, Dearborn, MI, USA) and transcardially perfused with 0.01 M PBS. The brains were removed and fixed in 4% paraformaldehyde for 24 h and transferred to 30% sucrose in 0.2 M PBS. After brains were saturated, they were snap-frozen on dry ice and coronal sections, 50 μm thick, were made with a sliding microtome. Sections were stored in 0.2 M PBS, 30% sucrose, and 30% ethylene glycol at −20°C. For viewing, cut sections were washed in PBS, mounted, and intrinsic GCaMP6 fluorescence was examined with epifluorescence microscopy (Nikon Eclipse 80i, Nikon Instruments, Melville, NY, USA). For viewing using confocal microscopy, additional cut sections were washed in PBS, mounted, and coverslipped in DAPI containing mounting media (Vector Laboratories, Burlingame, CA, USA). Fluorescent images were acquired with a Nikon A1-Rsi inverted confocal microscope using a 10x objective. DAPI labeled cells and electrode marker DiI were excited with 405nm and 560nm laser lines, respectively (Nikon A1-Rsi, Nikon Instruments, Melville, NY, USA).

QUANTIFICATION AND STATISTICAL ANALYSIS

Image Processing

A representative frame of baseline light levels in a dark environment, calculated from a mean of dark images collected over 1 minute, was subtracted from the raw data. All pixel time traces were individually detrended to remove any variations in light levels due to photobleaching, LED current drift, and nonuniformity across the skull. Reflectance changes in the 523nm, 595nm, and 640nm LED channels were used in combination to provide oximetric data using the Modified Beer-Lambert Law, described previously (White et al., 2011). Images in each contrast were smoothed with a Gaussian filter (5x5 pixel box with a 1.3 pixel standard deviation). The GCaMP6 fluorescent signal must be corrected for any contribution from vascular activity and varying concentrations of absorptive hemoglobin. Though the effects of hemodynamics will likely not mask the emission signals entirely, they will influence them. Common correction methods to calculate relative fluorescence changes include using a reference wavelength for applying subtraction and ratiometric techniques. We implemented a ratiometric correction algorithm (Equation 1) to correct fluorescent emission for any absorption by hemoglobin and deoxyhemoglobin using the reflectance channels at the GCaMP6 emission wavelengths (523nm LED) as a reference.

$$y(t) = \frac{I^{em}(t)}{I^{ref}(t)} \cdot \frac{I_0^{ref}}{I_0^{em}} \quad \text{(Equation 1)}$$

I^{em} refers to the detected fluorescent emission intensity. I^{ref} describes the measured reflectance changes at the emission wavelength. A single frame from the 628nm reflectance channel was loaded into Adobe Photoshop CC 2014 (Adobe Systems, San Jose, CA, USA) and all regions not corresponding to brain were manually painted white. The image was loaded back into MATLAB and used to create a binary brain mask. All subsequent analysis was performed on those pixels labeled as brain. Image sequences from each

mouse (as well as the brain mask for each mouse) were affine-transformed to a common atlas space (based on the Paxinos mouse atlas) using the positions of bregma and lambda. Global signal was not regressed from the data.

Electrophysiology Signal Processing

16-channel recordings were referenced to a ground wire positioned on the right hemisphere contralateral to the electrodes (2.3 mm Right of bregma, 0.9 mm anterior to bregma). To further verify that 16 channels spanned the depth of motor cortex and 12 channels spanned the depth of visual cortex (Figure 4A), we analyzed the spectral content of all channels. We found very similar spectral content in all 16 channels of motor cortex in all recordings, indicating that all channels were likely in cortex. In contrast, channels 13-16 in visual cortex exhibited far lower power than channels 1-12, indicating that 12 channels span the depth of visual cortex, and that channels 13-16 were in underlying white matter (and hence excluded from analysis). 60Hz notch filtering was applied to remove electronic noise from the data (Figure S6).

Correlation and Temporal Lags

As described in Figures 1B and 1C, conventional correlation analysis involves computation of the Pearson correlation, r, between the time series, $x_1(t)$, extracted from a seed region, and a second time series, $x_2(t)$, extracted from some other locus (single pixel or region of interest). Thus,

$$r_{x_1x_2} = \frac{1}{\sigma_{x_1}\sigma_{x_2}} \frac{1}{T} \int x_1(t) \cdot x_2(t) dt, \quad \text{(Equation 2)}$$

where σ_{x_1} and σ_{x_2} are the temporal standard deviations of signals x_1 and x_2, and T is the interval of integration. Here, we generalize the assumption of exact temporal synchrony and compute lagged cross-correlation functions. Thus,

$$r_{x_1x_2}(\tau) = \frac{1}{\sigma_{x_1}\sigma_{x_2}} \frac{1}{T} \int x_1(t+\tau) \cdot x_2(t) dt, \quad \text{(Equation 3)}$$

where τ is the lag (in units of time). In both optical and electrophysiological recordings, lagged correlation curves were computed between pairs of recordings (pixels and electrodes, respectively). The value of τ at which $r_{x_1x_2}(\tau)$ exhibits an extremum defines the temporal lag (equivalently, delay) between signals x_1 and x_2. The value of $r_{x_1x_2}(0)$ is the traditional zero-lag Pearson correlation. All pairs of temporal lags and zero-lag correlations define time-delay (TD) and functional connectivity (FC) matrices, respectively. In the imaging data, 16.8Hz temporal sampling density limits detection of empirical temporal delays to ~60ms; however, we apply parabolic interpolation to imaging-derived lagged cross-correlation curves to detect temporal delays shorter than the temporal sampling rate. There is strong agreement between empirical temporal delay matrices and temporal delay matrices computed using parabolic interpolation (Pearson r = 0.99 between measurements) in delta activity under anesthesia, as well as infra-slow activity measured in wake and anesthesia. The exception is delta activity during wake, where parabolic interpolation uncovers short temporal lags (+/−10 ms in Figure 1E) that cannot be measured empirically. Critically, wake delta activity temporal delays computed using parabolic interpolation are stable (Figure S2), agree with previous findings in the literature acquired with higher temporal sampling rates (Shimaoka et al., 2017), and agree with the present electrophysiological findings sampled at 300Hz (Figure 4C). Parabolic interpolation was only applied to the imaging data; electrophysiological temporal delays were computed empirically as the data was acquired at a much higher temporal sampling density. FC and TD matrices were computed over specific frequency bands by applying zero-phase filtering (fourth order Butterworth) directly to GCaMP6, hemoglobin, and electrophysiological (LFP) signals.

Group-level FC and TD matrices

In the imaging data, lagged-correlations were computed between every pair of pixels in the brain for each 5 minute run. FC and TD matrices computed over 5 minute runs were then averaged for each mouse across wake and anesthesia sessions. Separate averages computed for each 10-minute epoch allowed us to verify stability across time and mice (Figure S2). Occasionally, the spectral content of an awake imaging run contained delta signatures of sleep (Figure S6); these runs were omitted from the awake analysis, leading to a loss of 5.2% of the total wake imaging data collection. Group level FC and TD matrices are computed from the average of individual mouse FC and TD matrices over both days of imaging. A similar strategy was applied to compute FC and TD matrices in the electrophysiology data. Although the electrophysiological data was acquired continuously, to match the imaging analyses, we split the recordings into 5 minute epochs and computed FC and TD matrices in each epoch. Epochs were then averaged first within a mouse (wake and anesthesia), and then across mice, to produce Figures 4 and S2. As in the imaging data, we also used delta power to exclude likely periods of sleep from the wake electrophysiology (Figure S6). In the thirteen analyzed mice, 8.3% of total wake data was omitted due to putative sleep.

Group-level Phase-frequency Plots

Time series were extracted, in the imaging data, from visual and motor regions of interest (ROIs), shown in Figure 2. Then, in each 5 minute epoch of usable data, ROI time series were filtered into a double-octave frequency bin (0.02-0.08Hz ranging to 1.28-5.12Hz). For each 5 minute epoch and each double-octave frequency bin, the phase relationship between motor and visual time series was calculated by taking a Hilbert transform of each time series (as in Figure 4E) and computing the median instantaneous

phase delay. These phase relationships were then averaged first within, then across, sessions as described for the computation of FC and TD matrices. The same strategy was applied to compute phase-delay matrices for Figure S4.

Group-level Granger Causality (GC)

GC analysis was performed in the time domain using Anil Seth's GC toolbox (Barnett and Seth, 2014). Time series were extracted, in the imaging data, from visual and motor ROIs shown in Figure 2. These time series were then filtered into delta (1-4Hz) and ISA (0.02-0.1) frequency ranges, in anesthesia and wake. As GC does not lend itself to averaging over epochs, we concatenated 5 minute epochs of time series, in each frequency band, over sessions and mice. We then applied time domain GC analysis to these concatenated time series in each frequency band, where the auto-regressive model order was set to 150% of the lowest frequency in the frequency bin (e.g., 75 s for ISA, 1.5 s for delta), as recommended (Barnett and Seth, 2014). Statistically significant GC was found in every case ($p < 0.01$). GC results were identical over a range of model orders (75%–175% of the lowest frequency in the frequency bin). To address possible shortcomings in GC, we also verified that GC results are consistent with simpler, more interpretable metrics such as phase delays and temporal delays.

Current Source Density

Local field potential recordings can be confounded by the common reference electrode and passive volume conduction. One strategy for reducing the influences of these effects on LFP data is to apply a current source density (CSD) analysis, which amounts to computing a second spatial derivative over time series data. We computed one-dimensional CSD profiles over our linear recording arrays (in motor and visual cortices, respectively) using a three-point formula for approximation of the second spatial derivative:

$$D = \frac{d^2 f}{dx^2} \approx -\frac{[f(x-h) - 2f(x) + f(x+h)]}{h^2}, \quad \text{(Equation 4)}$$

where f is the voltage, x is the point at which D is computed, and h is the intercontact spacing on the linear array. For analysis of band-pass filtered signals, CSD was computed prior to band-pass filtering.

Statistical Significance

The high dimensionality of the presently analyzed data required the use of various non-parametric means for assessing statistical significance, described below:

(1) Statistical significance of correlations in the FC matrices in Figures 1D and 4B: Statistical significant of individual correlation values in the FC matrices computed using standard parametric methodology: by using a two-tailed Student's t-distribution for transformed Pearson r values. However, as there are many Pearson r values (dozens to tens of thousands) in each of the FC matrices, there is a multiple-comparisons problem. To address this issue, we take advantage of the fact that the correlations in these FC matrices are not independent, and apply the Laplacian estimate of the Bayesian information criterion to the eigenspectra of these matrices to determine the underlying dimensionality. On this basis, the underlying dimensionality of the FC matrices in Figure 1D is found to be 9. We then apply a Bonferroni-correction on model order to determine correlation values with $p < 0.005$, demarcated by the asterisk in Figure 1D. The same principle is applied in Figure 4B, except as the experimental question aims to identify laminar specificity, we use a more conservative approach, applying a Bonferroni-correction on layers (6*6 = 36; correlation matrices in Figure S4 demonstrate channels within layers are not independent) such that only temporal correlations with $p < 0.001$ are shown as significant (the model order approach only requires a multiple comparisons correction of 9). We note that the purpose of this computation is not to make any strong claims about FC (which is not the focus of this paper), but merely to provide an estimate of the most consistent correlation values.

(2) Statistical thresholding of temporal delays in Figures 1E and 4C: Surrogate temporal delays were computed for each pair of imaging traces/recordings by randomly phase-permuting filtered time series prior computation of lagged correlations, resulting in a null-distribution of temporal delays. The empirical distribution of temporal delays between each pair of channels (recall TD was computed for each mouse over 5-minute epochs) was then compared to the null-distribution with the Kolmogorov-Smirnov test. To address multiple comparisons, for the TD matrices in Figure 1E, we again computed model order as described above in (1), and found that the model order of these TD matrices is 9. We then applied a Bonferroni-correction on model order to determine temporal delay values with $p < 0.005$, such that non-significant values (of which there are very few) are shown in gray. For Figure 4C, we applied the same more conservative approach ($p < 0.001$) as described for laminar FC matrices in (1) above.

(3) Statistical differences in TD matrices in Figure 1E: As described in the computation of group-level FC and TD matrices, group-level TD matrices are computed by averaging TD matrices computed over 5 minute epochs first within then across mice. To test for statistical significance between group-level TD matrices, average TD matrices from each of the 14 mice were randomly permuted (either over ISA versus delta, or wake versus anesthesia). We then computed a null-distribution of magnitude difference (Euclidian distance) between surrogate group-level TD matrices. On the basis of this null-distribution, we conclude that differences in the TD matrices in Figure 1E are statistically significant ($p < 0.001$), both across ISA versus delta, as well as across wake versus anesthesia.

(4) Statistical differences in lag projections in Figure 2A: Same strategy as (1) above, except surrogate group-level TD matrices were transformed into lag projections (through column-wise means) to produce surrogate group-level lag projections. The null-distribution was then computed as a vector Euclidian distance between lag projections, treating the images as 1-dimensional vectors (e.g., one number per brain pixel). On the basis of this null-distribution, we conclude that differences in the lag projections in Figure 2A are statistically significant ($p < 0.001$), both across ISA versus delta, as well as across wake versus anesthesia.

(5) Statistical differences in FC and TD matrices in Figures 4B and 4C: Precisely the same approach outlined in (1) above, applied to electrophysiology FC and TD matrices.

(6) Statistical approach in Figure 2D: The shaded regions show the 95% confidence intervals around the median value of the instantaneous phase delay between visual and motor cortices across double-octave frequency bins.

(7) Statistical significance of phase-amplitude coupling (PAC) in Figures 4E and 4F: The null-hypothesis for the phase-amplitude histograms shown in Figure 4F is a uniform distribution. Therefore, we tested for significant PAC by using the Kolmogorov-Smirnov test to compare the empirical PAC histograms to a uniform distribution, resulting in a p value < 0.001. We also applied a second permutation-based test of PAC using modulation index as described in Canolty et al. (2006). In essence, PAC can be thought of as a vector on a circle depicting a preferred phase relationship between a pair of signals; the length of this vector is the modulation index. By randomly permuting the underlying signals, a surrogate PAC vector is computed, along with its length (e.g., a surrogate modulation index). The null-distribution of surrogate modulation indices provides a test of statistical significance. By this measure as well, the presently observed PAC (imaging and electrophysiology) is highly significant ($p < 0.001$).